

Velocity Map Imaging Spectrometer Optimized for Reduction of Background Electrons from Scattered UV Light

Nicolas Ladda,^{1, a)} Fabian Westmeier,¹ Sagnik Das,¹ Wilfried Dreher,² Simon T. Ranecky,¹ Tonio Rosen,¹ Krishna Kant Singh,¹ Till Jakob Stehling,¹ Sudheendran Vasudevan,¹ Hendrike Braun,¹ Thomas Baumert,¹ Jochen Mikosch,¹ and Arne Senftleben^{1, b)}

¹⁾ *University of Kassel, Institute of Physics, Heinrich-Plett-Str. 40, 34132 Kassel, Germany*

²⁾ *Schülerforschungszentrum Nordhessen SFN, Parkstr. 16, 34119 Kassel, Germany*

Velocity map imaging spectroscopy is a powerful technique for detecting the momentum distribution of photoelectrons resulting from the ionization of atoms, molecules, clusters, or surfaces. However, when used with ultraviolet light sources, scattered photons can lead to the emission of photoelectrons from the spectrometer's electrodes, giving rise to severe noise superimposing the desired signal. We present a velocity map imaging spectrometer optimized to reduce such unwanted background signals. The primary modifications to the conventional design include spectrometer electrode geometries with small cross sections exposed to the scattered photons, blocked pathways for photoelectrons from the electrodes to the detector, and the incorporation of optical baffles to confine the solid angle of scattered light. Compared to a conventional design optimized solely on the spectrometer's photoelectron momentum resolution, we have achieved the elimination of 99.9 % of the background noise without noticeably compromising the resolution. Note that most of the improvements were achieved without the necessity of high-grade windows, reducing the sensitivity to window degradation by UV light. We give general guidelines on efficiently coping with the long-standing experimental problem of electron background originating from scattered light by considering it already in the design stage of a new spectrometer.

I. INTRODUCTION

Velocity map imaging (VMI) spectroscopy¹ represents a powerful experimental method for detecting the momentum of charged particles. In this technique, static electric fields map particles with the same charge and momentum vector onto the same point on a detector, independent of their precise initial position in the source volume.² In the conventional configuration, a position-sensitive detector, typically the combination of a micro-channel plate (MCP), a phosphor screen, and a digital camera, measures a two-dimensional (2D) projection of the momentum distribution. This scheme works well for distributions that exhibit cylindrical symmetry,³ where the full three-dimensional momentum distribution can be reconstructed using Abel inversion.^{4,5} Although there are many methods implementing Abel inversion, not all of them are general and can only be used in certain cases. The pBasex algorithm, for example, is not a general Abel inversion technique and requires, in addition to cylindrical symmetry, that the signal can be constructed from Legendre polynomials. However, this is advantageous for VMI photoelectron data, as this restriction often eliminates some of the noise in the data.⁶ The VMI method is typically applied to photoionization experiments (see below) or collision experiments involving charged particle beams.^{7,8} Different variants of the conventional scheme are routinely used, particularly for situations without cylindrical symmetry. In slice imaging,

the detector is activated only for a short time window, such that exclusively particles with initial momentum parallel to the detector are recorded.^{9–11} In tomographic reconstruction, the electric field of a linearly or elliptically polarized laser pulse is rotated and a set of photoelectron angular distributions (PADs) are recorded at different rotation angles.^{12–14} In three-dimensional (3D) imaging, time- and position information of particle impact on the detector is determined using two digital cameras with different integration times,¹⁵ cameras with high time-resolution,^{16,17} the correlation of independently determined camera and time-of-flight information,^{18–20} or delay-line or strip anodes instead of a phosphor screen.²¹ Meanwhile, also double-sided VMI spectrometers are used to record photoelectrons and -ions in coincidence.²²

The first imaging spectrometer capable of measuring the entire momentum distribution simultaneously was constructed by Chandler and Houston in 1987, utilizing a repeller electrode and a grounded grid electrode.²³ Subsequently, Eppink and Parker incorporated a third electrode (extractor) into the configuration. Their setup was analogous to the time-of-flight spectrometer developed by Wiley and McLaren.²⁴ However, in contrast to the grid electrodes used in the setup of Wiley and McLaren, the solid electrodes with apertures used by Eppink and Parker introduced inhomogeneous electric fields, significantly enhancing the momentum resolution.¹ After this pioneering work, various researchers have contributed to advancing the technology by adding additional electrodes to improve the resolution.^{25–27} Some researchers have optimized the VMI design, enabling the measurement of electrons with high kinetic energy of up to 1 keV.^{28,29} Others have implemented Einzel lenses to enlarge the dis-

^{a)} Electronic mail: Nicolas.Ladda@uni-kassel.de

^{b)} Electronic mail: arne.senftleben@uni-kassel.de

tribution on the detector,^{30,31} or optimized the shape of the electrodes to increase the resolution further.³²

The VMI technique is often used to investigate the momentum distribution of photoelectrons, which can be used to study photoionization processes.^{33–35} Combined with femtosecond laser pulses, ultrafast dynamics can be observed.^{36,37} In the context of chiral molecules, VMI is used to measure the Photoelectron Circular Dichroism (PECD), an enantiomer-sensitive effect of the photoelectron momentum distribution.^{38,39}

With UV laser pulses, many molecules can be excited from the ground state with one photon and subsequently ionized with a second photon.⁴⁰ However, photons of sufficiently high energy for such a scheme (> 5 eV) can generate a lot of background noise.^{41–43} In VMI spectroscopy, the light beam usually enters the spectrometer chamber through a window, causing some light to scatter. The scattered photons have enough energy to overcome the work function of metals that are used for the spectrometer electrodes, which are often made of aluminum, steel, or copper, all of which have a work function of less than 5 eV.^{44–47} Gold plating of the electrodes should result in a surface work function greater than 5 eV. However, the work function of gold is also reduced below 5 eV when exposed to air.⁴⁸ The work function of other metal-oxides or graphite is also reduced by the exposure to air^{49,50} or surface roughness.⁵¹ Recently, electrodes coated with the nanostructured highly absorbing material Vantablack were employed in a VMIS to reduce the emission of electrons.⁵² This promising result suggests another possibility for reducing the background electron signal, which could be integrated with the other techniques outlined in this work.

The usual approach to cope with scattered light is an optical baffle system, an approach inspired by astronomical telescopes.⁵³ The optical baffle system aims to block pathways from the window to the surfaces in the spectrometer. However, limitations arise from multiple scattering events at the optical baffle system itself, in particular at grazing incidence and the sheer number of incident photons.

Due to the low ionization rate inherent to dilute gas-phase targets, the rate of useful events in such experiments is often very low. Therefore, a high photon flux is required, with a high probability of creating background electrons that arrive on the detector simultaneously with the desired electrons. Therefore, scattered light is a long-standing challenge in photoelectron spectroscopy involving deep-UV or vacuum-UV (VUV) laser pulses.

Here, we present a velocity map imaging spectrometer (VMIS) that suppresses background electrons resulting from scattered UV light, mostly via an optimized geometry of the spectrometer electrodes. We have identified key design considerations that reduce the background, which we present in order of their significance. Note that the electrode material or the vacuum windows do not appear to be the main factors in solving the problem of background signal resulting from UV photons.

II. OPTIMIZATIONS FOR BACKGROUND REDUCTION

When designing a VMIS, momentum resolution is often the primary concern, and the ability to suppress background from scattered light is neglected. This issue is then addressed later, for example, by using high-quality vacuum windows to minimize scattering.⁵⁴ The problem with this approach is that the laser windows often degrade over time, either by the formation of adhesive layers or by damage from the UV laser beam, in particular, color center formation. Our strategies reduce the background noise for a VMIS to acceptable levels, even if the windows are a significant source of scattered photons.

Our VMIS consists of four electrodes: ground, extractor, repeller, and pusher plates, as illustrated in Figure 1a. The electrodes are insulated from each other by Teflon rods. The screws visible above the pusher plate in the figures are also made of Teflon.

The pusher plate was initially installed to enable coincidence detection of ions in a time-of-flight spectrometer, but turned out to be crucial for the low-background VMIS (see below). The detector comprises a 75 mm diameter, funnel-type MCP⁵⁵ with a P43 phosphor screen. To compensate for magnetic stray fields, we use Helmholtz coils positioned outside the vacuum chamber. This eliminates the need for mu-metal shielding with apertures that allow light and particles to reach the interaction area. Avoiding these apertures might reduce light scattering, resulting in fewer background electrons.

The fourth harmonic of a femtosecond titanium-sapphire laser was used as a light source. The laser pulses have a central wavelength of 197 nm (6.26 eV photon energy) and a pulse energy of 1 μ J at a repetition rate of 3 kHz. The collimated beam diameter and pulse duration are approximately 3 mm ($1/e^2$) and 100 fs (FWHM), respectively. For additional testing, the background signal caused by the third harmonic of the titanium sapphire laser with a central wavelength of 263 nm (4.7 eV) was also used, where the collimated beam diameter and pulse duration were about 4 mm ($1/e^2$) and 30 fs (FWHM), respectively. We focus on the results for the fourth harmonic, since this wavelength caused much more background noise than the third harmonic.

For this investigation, the unfocused laser beam was passed through the vacuum chamber without a target (pressure: 10^{-8} mbar), to assess the background from scattered light. The initial windows were made of low-grade CaF_2 , which causes a lot of scattering. For quantitative comparison, images of the background signal were taken under the same conditions, such as MCP voltage, camera exposure time, and number of averaged images. Furthermore, we aligned the laser beam to the same path between measurements, as misalignment can have a strong influence on the background signal.

We started our investigations with a resolution-optimized VMIS (see Figure 1a) that was designed with the help of electron trajectory simulations with SIMION 8.0.8,⁵⁶ a standard widespread tool for developing ion

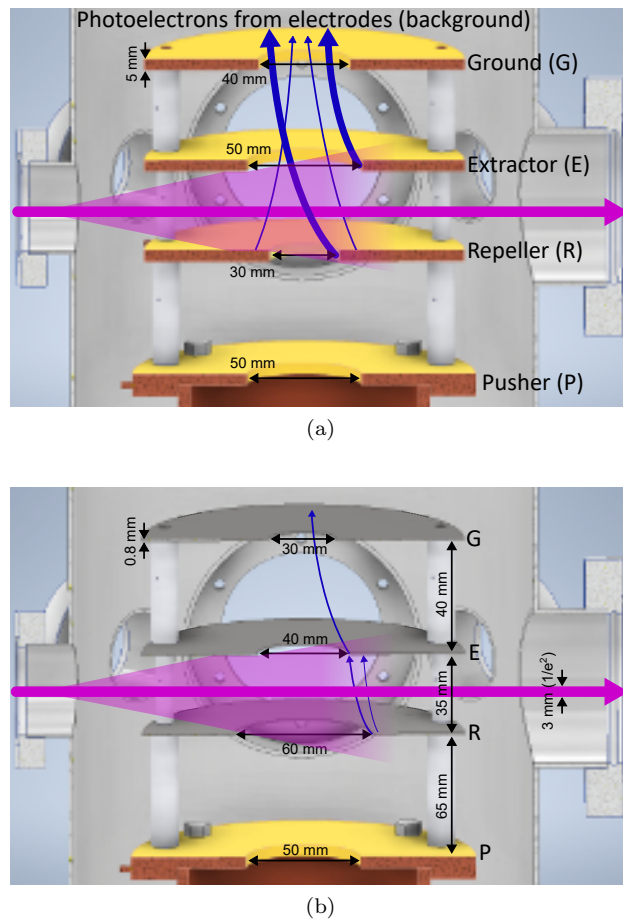


FIG. 1. Comparison of VMIS with different electrode thicknesses. The magenta-colored arrow indicates the laser beam and its direction, while the magenta-colored cone visualises the scattered photons hitting the electrodes. The opening angle of the cone was drawn so that rays that do not hit the critical inner parts of the electrodes are excluded. (a) shows the resolution-optimized VMIS with thick electrodes, which lead to the creation of a lot of electrons (big blue arrows) near the electrode apertures. (b) shows a VMIS with thin electrodes and a better choice of electrode apertures. Here, due to the smaller cross-section, fewer electrons are created from the electrodes (small blue arrows), and most are blocked by the extractor plate, reducing the background signal.

and electron optics. As in many other VMI spectrometers, our optimization resulted in relatively thick electrodes, in our case 5 mm thick. As a precaution to cope with scattered light, gold-plated copper electrodes were employed since gold should have a higher work function than steel or aluminum. The resulting background measurement is depicted in Figure 2a. A high, nonspecific signal is seen that overshadows any other signal. The visual shape of this signal responds to changes in the voltages on the electrodes. Therefore, we conclude that most of the background consists of electrons rather than photons impacting the front MCP of the detector, generating signals.

Interestingly, we also observed a similar background

signal when using the third harmonic. However, this signal, even though exhibiting a similar distribution, was weaker than the one caused by the fourth harmonic by about a factor of 5, which can be explained by the lower amount of scattering for longer wavelengths.⁵⁷ The reason that photoelectrons are generated even by the third harmonic is that a gold surface exposed to air suffers from adsorption, which is not easily removed under vacuum conditions and drastically reduces the work function.^{48,58}

We quantify the improvement by comparing the signal strength of the background noise before and after the implementation of each design modification. The following data processing procedure is conducted in three steps: First, the minimum value of each image is determined and subsequently subtracted from each pixel. Then, the value of each pixel is divided by the maximum value across all images. Finally, the result is multiplied by 100. Consequently, the image of the initial design had pixel values ranging from 0 to 100 (Figure 2a). Images of the adapted designs have values between 0 and < 100 (Figure 2b), demonstrating the extent to which background noise is reduced with each optimization.

A. Spectrometer design

We assume that the inner rim of the thick electrodes constitute the most significant source of background signal in Figure 2a, as the cross-section exposed to the incident light direction is high (see schematic light ray traces illustrated as a magenta-colored cone in Figure 1a). Moreover, light that hits the surface of the electrodes, in particular the top of the repeller electrode, does so under a grazing angle of incidence, which reduces its absorption significantly.

Photoelectrons created at the rims are accelerated straight onto the detector, resulting in severe background noise. Therefore, the rim's cross-section should be small. This can be achieved by using wedge-shaped electrodes, with the thickness decreasing towards the aperture, or simply thin electrodes. In our improved design, we used plan-parallel thin plates (0.8 mm thick), made of stainless steel (see Figure 1b).

Furthermore, the electrodes in a VMIS are usually designed such that the aperture diameter in the extractor plate is at least as large as that in the repeller plate. However, to reduce background noise, the opposite is advisable. Liu *et al.* have already suggested that most of the background signal comes from the repeller plate.⁵⁹ We use a diameter of 60 mm in the repeller and 40 mm in the extractor plate (see Figure 1b). Most electrons emitted from the repeller plate are then blocked by the extractor plate instead of reaching the detector (see Figure 1). However, when using a large hole in the repeller electrode, an additional electrode below the repeller plate is crucial.⁶⁰ This pusher electrode helps to improve the resolution of the VMIS by a factor of approximately two while also helping to reduce the background signal, ac-

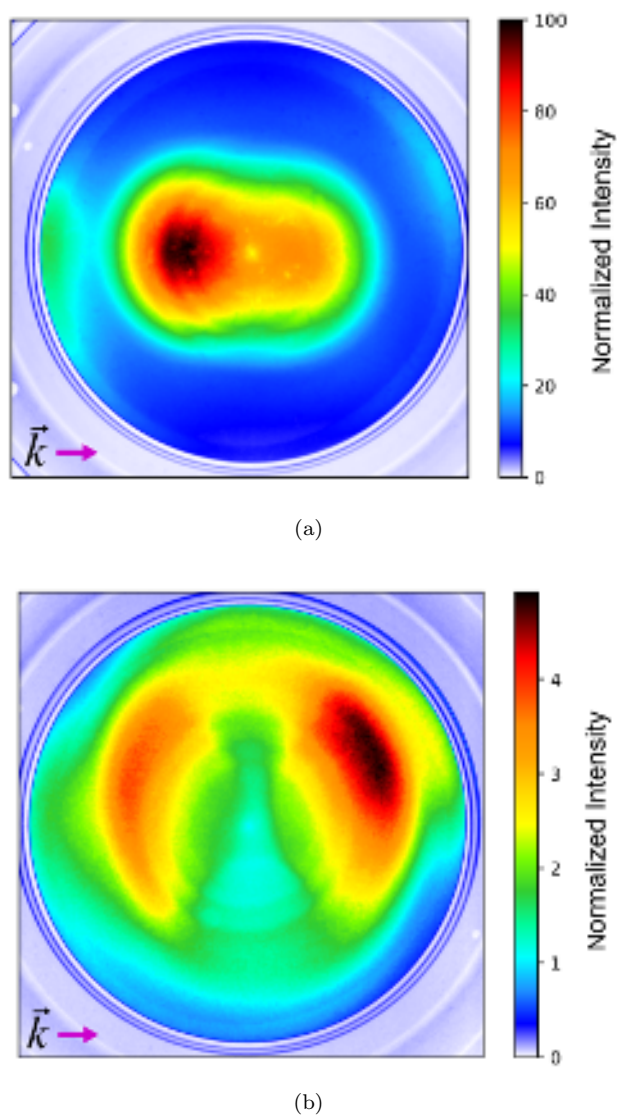


FIG. 2. Comparison of the background signal measured without target gas under the same conditions between the two VMIS designs depicted in Figure 1. (a) shows the background signal for the initial resolution-optimized design. (b) shows the background signal for the improved design, with thinner electrodes and a larger aperture in the repeller than in the extractor. \vec{k} depicts the propagation direction of the light pulses. The color scale indicates the normalized intensity of the background signal calculated by the procedure described in the text.

according to our SIMION simulations (see Figure 3).

In our improved design of the VMIS, the distance between the pusher and repeller is 65 mm, while the repeller–extractor and extractor–ground distances are 35 mm and 40 mm, respectively. The aperture dimensions of the electrodes are as follows: 50 mm for the pusher, 60 mm for the repeller, 40 mm for the extractor, and 30 mm for the ground plate. The following voltages were found to optimize our spectrometer’s resolution for electrons while directing all electrons emitted from the re-

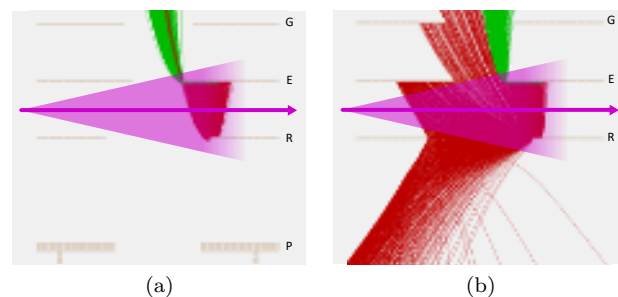


FIG. 3. Comparison of simulated electron trajectories (a) with and (b) without pusher electrode. The red and green lines represent electrons ejected from the repeller and the extractor plate, respectively. With the pusher electrode (P) more electrons emitted from the repeller plate are directed into the extractor plate, reducing the background signal.

pellor plate into the extractor plate: extractor -1305 V, repeller -1700 V, and pusher -3000 V. However, the exact distances between the electrodes and the aperture sizes as well as the voltages should be optimized for each spectrometer design individually. It is also possible to add additional lenses to increase the momentum resolution.

Notably, after implementing the improvements in the electrode design, the highest pixel value was less than 5, indicating that more than 95% of the background noise has successfully been removed (see Figure 2).

B. Optical baffles

The purpose of optical baffles is to largely block the path of scattered light between its source, in our case the vacuum window traversed by the laser, and the sensitive surface, the spectrometer electrodes. Importantly, since multiple scattering can occur, one has to find a good compromise between blocking scattered light and not cutting too much into the wings of the laser beam, which typically has a Gaussian spatial profile. We use a modular, vacuum-compatible design for the optical baffle system. One element consists of three pieces: a cylinder, a cone, and a base plate (see Figure 4a, where the assembly is shown). The edges of the cone are as thin as possible (knife-edge) to minimize specular reflection from the edge towards the spectrometer.

To avoid clipping of the beam on the knife edge, we designed the aperture of the conical part to be 9 mm in diameter, which is about three times larger than the collimated beam diameter (3 mm).

We usually operate our VMIS in a back-focussed arrangement, in which the collimated laser beam is transmitted through the vacuum chamber via an entrance and exit window and then back-reflected by a concave spherical mirror placed in front of the exit window, which produces a focus in the source volume of the VMIS.

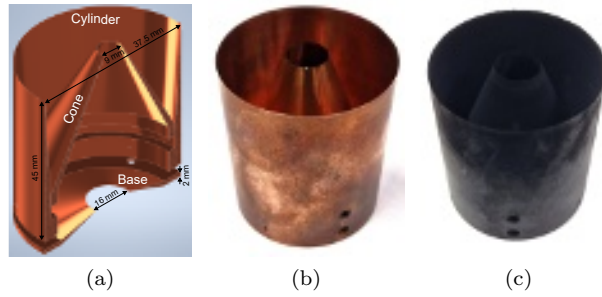


FIG. 4. Modular design of the optical baffles (a), consisting of a cylinder, a conical piece, and a base plate. Optical baffles before (b) and after (c) the blackening process.

This arrangement has advantages over other configurations: (1) Due to the focusing from a reflecting surface, there is no chromatic aberration. Two collimated laser beams with different wavelengths are focussed at the same position, which is important for multi-color pump-probe experiments. (2) No astigmatism is introduced, and a shorter focal length is possible compared to folded beam paths. (3) By placing the focussing mirror outside the vacuum, it is easily accessible for alignment and replacement. (4) By reflecting of the mirror under normal incidence, it is ensured that the polarization stays circular, which is an important aspect for many of our experiments.

To block scattered light both from the incoming and the back-focussed beam, one of the optical baffle elements described above (see Figure 4a) is placed on each side of the VMIS stack, as seen in Figure 5a. The cones are facing inwards to bring their aperture as close as possible to the interaction regime and confine the solid angle of scattered light as much as possible.

The optical baffles must exhibit high absorption in the UV and be conductive enough to avoid charge build-up, to not disturb the spectrometer fields. A material that fulfills these criteria is copper covered by a thin layer of cupric oxide (CuO) with a dendritic surface structure.⁶¹ A wet etching technique can easily create the oxide layer.^{61–63}

First, it is necessary to remove any larger dirt particles from the copper parts with water and soap. For the primary cleaning step, acetone and isopropanol should be used (in combination with an ultrasonic cleaning bath if necessary). Afterwards, the pieces should be soaked in concentrated acetic acid at approximately 50°C for 3–5 minutes. This will remove most residual oxide layers from the surface without affecting the copper. It is advised that these two steps are repeated until the surface appears thoroughly cleaned, ending with the acetic acid bath.

In the next step of the process, the copper pieces are etched with nitric acid (20%) at a temperature of 50°C for a duration of between 60 and 90 seconds. This step removes any residual oxides and roughens the surface of the

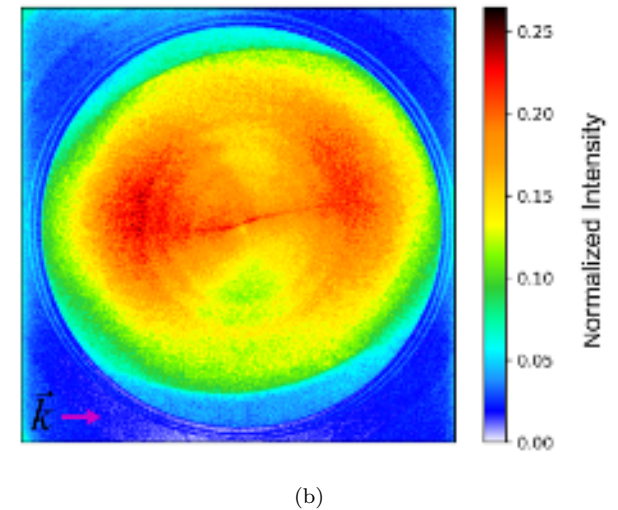
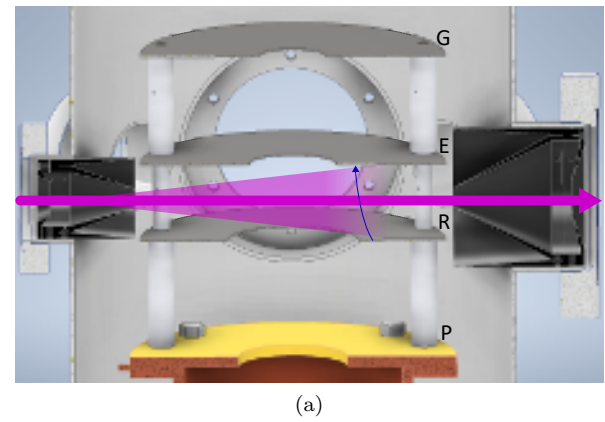


FIG. 5. Influence of the optical baffles on the background noise. (a) shows the spectrometer with the optical baffles installed, which confine the solid angle of scattered light entering the spectrometer. Now the magenta-colored cone of scattered light was drawn to represent the opening angle allowed by the first baffle. (b) shows the background signal for this design.

pieces. Subsequently, the copper pieces are washed several times in distilled water to remove all traces of nitric acid. It is essential to note the importance of this step, as any residual acid can have a significantly detrimental effect on the quality of the final result. It is advisable to employ a two-water bath system, with the second water bath being slightly basic (by the addition of NaOH). After etching, the final step should be carried out without delay in order to avoid the re-formation of new oxide layers, which would also compromise the quality of the results.

In the final step of the process, the etched copper pieces are oxidized by potassium persulfate (20 g/L) in a 60 g/L NaOH solution at 55°C. It is critical to maintain a temperature below 60°C (to avoid decomposition of the persulfate) and to ensure that stirring is not excessive.⁶² The reaction is self-limited and typically takes 25 min-

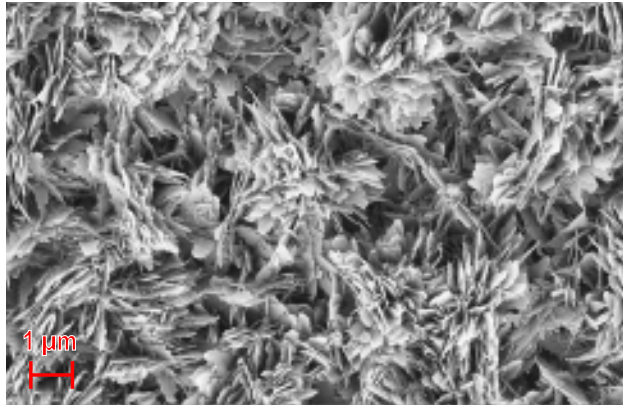


FIG. 6. Surface structure of the blackened optical baffle imaged with an SEM. The surface was coated with a minimal amount of gold to increase secondary electron yield. The dendritic cupric oxide crystals are less than 100 nm thin and oriented randomly.

utes to complete. After additional washing and drying in a drying cabinet, the outcome of this reaction is a surface that is characterized by its extremely high degree of blackness and its high UV absorption capabilities.^{61,63}

For the first cleaning process and the subsequent etching with nitric acid, an aluminum holder with holes was used to suspend the copper piece in the solution. Aluminum is not affected by the solvents and acids. The holes should be large enough so that they do not block any of the critical copper surfaces. Aluminum, however, is particularly poorly suited for the blackening step, as it will be oxidized too. For this step, stainless steel or copper itself can be used as a support cage. If possible, the pieces can also be held with aluminum or copper wires for the corresponding step, but we have found that connecting and removing wires can be difficult. Further information can also be found in the thesis of Owen Clarkin.⁶¹

We examined the cupric oxide surface by scanning electron microscopy (SEM). Figure 6 presents SEM images of the surface structure of the blackened optical baffles. To enhance the signal in the electron microscope, a minimal amount of gold was sputtered onto the surface of a blackened piece that was not used in the VMI. A comparison with unsputtered samples revealed that this process did not affect the underlying structure. It is evident that the surface is composed of thin (less than 100 nm) but elongated cupric oxide crystals, which are oriented in an irregular pattern. This dendritic structure facilitates light absorption with high efficiency.^{61,63}

In Figure 5, the VMIS design incorporating optical baffles and the corresponding background noise measurement are presented. The confinement of the solid angle of scattered light leads to a reduction in the electrode surface area exposed to scattered photons, consequently diminishing the number of photoelectrons near the electrode apertures. This requires a sufficient distance be-

tween the repeller and the extractor electrode, while positioning the baffles as close as possible to the electrode plates. In the case of the VMIS presented here, the gap between both electrodes is 35 mm wide, while the electrodes themselves have a diameter of 140 mm. The distance between the baffles and the electrode plates is 2-3 mm. Additional SIMION simulations showed that the grounded optical baffles can harm the resolution of the VMIS if the width (outer radius minus inner radius) of the electrode plates is smaller than the distance between repeller and extractor. This reduces the electrode's ability to block the altered electrostatic field by the optical baffles.

Our measurements under defined conditions (see above) show that the incorporation of optical baffles in combination with the described geometrical modifications of the spectrometer electrodes results in a substantial reduction of background signal, with about 99.75% of the noise being suppressed as compared to the initial design (see Figure 5b). However, the laser beam must be aligned precisely through the optical baffle system to minimize scattering originating from clipping.

Some of the faint features in the image might originate from ionization of residual gas in the vacuum chamber by the collimated laser beam. The central structure in the image could be the result of bad focusing conditions (unfocused laser beam) and not optimized voltages on the electrodes of the VMIS. These signals can only be observed since the background signal from photons hitting the electrodes is low enough, which means that the background reduction might even be higher than stated here

C. Windows

The utilization of high-quality vacuum windows is beneficial in reducing the amount of scattering, with calcium fluoride (CaF_2) and magnesium fluoride (MgF_2) being particularly effective materials due to their high UV transmission. A low scattering rate is especially important for the deep-UV regime, since scattering scales with the inverse wavelength to the fourth power.⁵⁷

Since our experiments demand precise control over light polarization, using a birefringent material such as MgF_2 (even under z-cut) or placing the windows at the Brewster angle poses a challenge.

Crystal purity is an important factor in minimizing both scatter and window degradation. In addition, it is recommended that the surfaces of the crystal be polished to a low roughness in order to reduce scattering further.

We use 1.3 mm thick, 25 mm diameter optically polished VUV-grade single crystal CaF_2 as vacuum windows (Korth Kristalle), which we embedded with UHV compatible glue into a recess in a CF40 flange. We took care to align the laser beam as parallel as possible to the surface normal of the windows. This was done to minimize detrimental back reflections at an angle.⁵⁴

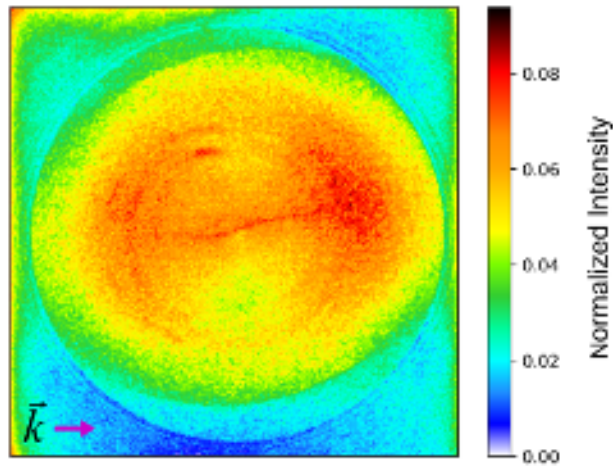


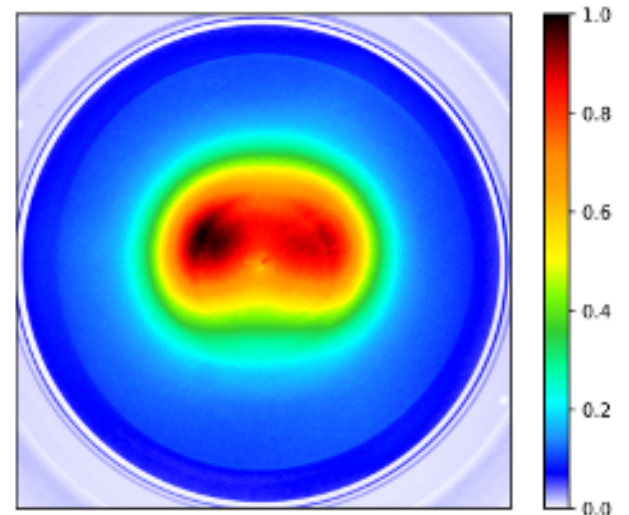
FIG. 7. Background signal after all improvements (electrode design, optical baffles, and high-grade vacuum windows). The background level has been reduced by more than a factor of 1000 compared to the initial design (compare Figure 2a)

With the high-quality windows added to the modifications described above, we eliminate 99.9 % of the initial background signal (see Figure 7), but the improvement is only a factor of three compared to the poor-quality windows. This is especially interesting since windows are prone to degradation over time due to laser-induced damage or accumulation of contamination on the surfaces.

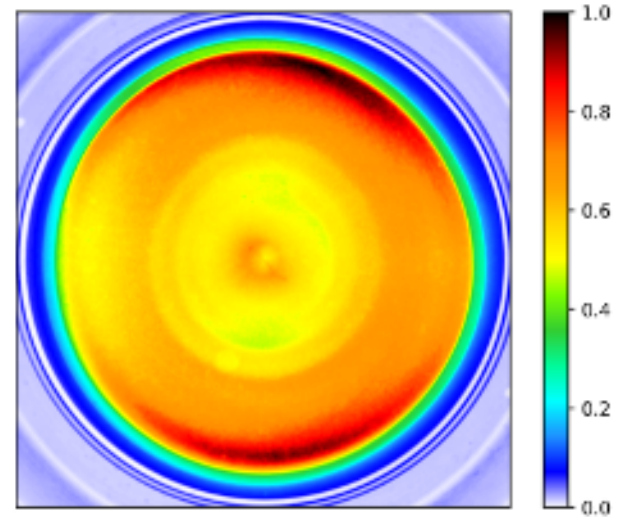
III. RESULTS

The improved VMIS featured a background signal that is more than 1000 times lower than that of the initial design. By determining the number of background electrons and the total number of photons in each laser pulse, we calculated that, on average, we create 4 electrons per 10^{12} photons of 197 nm and about 2 electrons per 10^{14} photons at 263 nm. This translates to about 4 electrons per pulse of 197 nm and 0.06 electrons per pulse of 263 nm in our experiment. Again, we see that background electrons become particularly problematic for shorter wavelengths. However, for the optimized spectrometer, the increase in background noise going to short wavelength can no longer be explained by an increasing scattering rate.

Figure 8 presents a comparison of a 1+1 Resonance-Enhanced Multi-Photon Ionization (REMPI) photoelectron momentum distribution of fenchone with 197 nm wavelength femtosecond pulses. Image (a) illustrates the recorded data obtained from the previous spectrometer design, in which a pronounced background signal is prominently visible in the center. The primary signal is barely perceptible. In contrast, image (b) was recorded using the novel setup, where virtually no background sig-



(a)



(b)

FIG. 8. Comparison between measurements of fenchone taken with the femtosecond laser pulses centred at 198 nm before (a) and after (b) implementing the changes to reduce background signal.

nal is visible. This has been achieved in a back-focusing geometry, where the laser beam passes through the experimental chamber twice. A further reduction of background is to be expected in a forward-focusing arrangement. For both measurements, the molecule was brought into the gas phase by an effusive inlet, and the pressure was about $5 \cdot 10^{-6}$ mbar.

To check the resolution of the new VMIS, photoelectrons from multi-photon ionization of xenon with the third harmonic of a nanosecond Nd:YAG laser (355 nm wavelength) were measured. The recorded detector image (2D projection of the photoelectron momentum distribution) and the corresponding photoelec-

tron spectrum, which was obtained by Abel inversion with the rBasex algorithm from the PyAbel package, are depicted in Figure 9.⁶ The measured resolution for the background-optimized VMIS design is $\Delta E_{FWHM}/E = 4.7\%$ at a kinetic energy of 1.9 eV, comparable to the previous resolution-optimized design. Further improvements on the resolution could be made by adding more lenses to the setup,^{25–27} which should not harm the background reduction properties.

The FWHM of the Abel-inverted signal is approximately 7 pixels. A single event generates a signal with an FWHM of approximately 4 pixels, indicating that the VMIS is operating close to the resolution limit of the detector. Consequently, the design adaptations made to minimize background signal do not significantly compromise the resolution of the VMIS.

IV. CONCLUSION

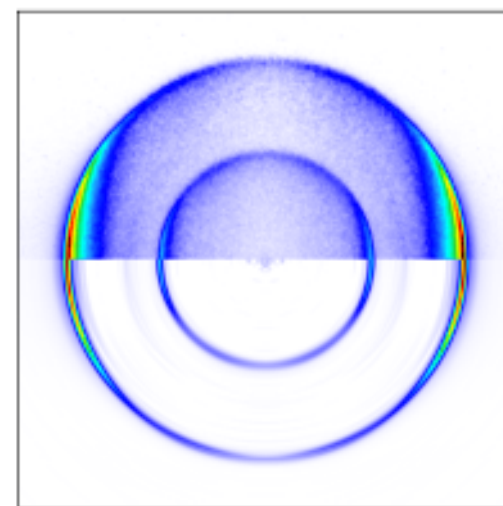
We present a VMIS design optimized to reduce photoelectron background originating from scattered UV photons. We found the largest potential for background reduction in the geometry optimization of the spectrometer plate electrodes and the installation of an optical baffle system. Specifically, the utilization of thin electrodes and the blocking of background electrons by the extractor are recommended. Installation of high-grade laser windows at the vacuum interface can reduce the background signal further, but their effect becomes comparatively small when the other measures are implemented. Taking the relatively small effect of good vacuum windows into account, we think that our design will also be relevant for spectrometers operating with VUV light, that usually do not have windows anyway. We have experimentally demonstrated that the background-optimized VMI design still features a good momentum resolution that is limited by the detector. The background signal of the final design was found to be more than 1000 times lower than that of the resolution-optimized VMIS.

ACKNOWLEDGMENTS

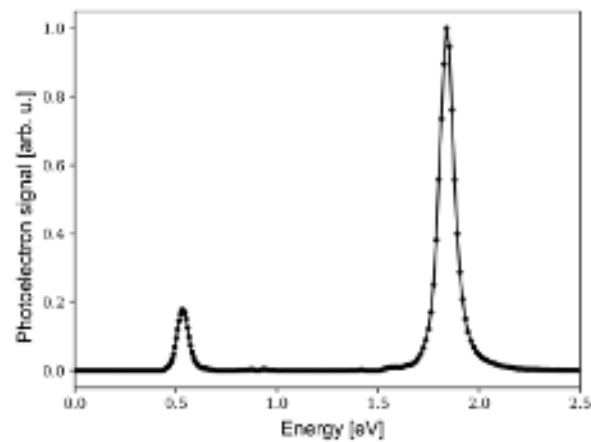
Financial support from Deutsche Forschungsgemeinschaft (DFG, German Research Foundation) – project number 328961117 – SFB 1319 ELCH is gratefully acknowledged. JM gratefully acknowledges support from the DFG within a Heisenberg professorship (project number 470414645).

DATA AVAILABILITY

The data that support the findings of this study are available from the corresponding author upon reasonable request.



(a)



(b)

FIG. 9. Photoelectron momentum distribution of xenon (a) and the extracted photoelectron kinetic energy spectrum (b), as recorded with the third harmonic of a nanosecond YAG laser (355 nm) with the background-optimized VMIS. A momentum resolution of $\Delta E_{FWHM}/E = 4.7\%$ was found. The upper half of the image in (a) shows the raw data, while the lower half represents the Abel-inverted data.

¹A. T. J. B. Eppink and D. H. Parker, “Velocity map imaging of ions and electrons using electrostatic lenses: Application in photoelectron and photofragment ion imaging of molecular oxygen,” *Rev. Sci. Instrum.* **68**, 3477–3484 (1997).

²D. H. Parker and A. T. J. B. Eppink, “Velocity map imaging: applications in molecular dynamics and experimental aspects,” in *Imaging in Molecular Dynamics*, edited by B. J. Whitaker (Cambridge University Press, 2009) pp. 20–64.

³A. T. J. B. Eppink, S.-m. Wu, and B. J. Whitaker, “Reconstruction methods,” in *Imaging in Molecular Dynamics*, edited by B. J. Whitaker (Cambridge University Press, 2009) pp. 65–112.

⁴G. A. Garcia, L. Nahon, and I. Powis, “Two-dimensional charged particle image inversion using a polar basis function expansion,” *Rev. Sci. Instrum.* **75**, 4989–4996 (2004).

⁵Mikhail Ryazanov, *Development and implementation of methods for sliced velocity map imaging. Studies of overtone-induced*

dissociation and isomerization dynamics of hydroxymethyl radical (CH₂OH and CD₂OH), Ph.D. thesis, University of Southern California (2012).

- ⁶D. D. Hickstein, S. T. Gibson, R. Yurchak, D. D. Das, and M. Ryazanov, "A direct comparison of high-speed methods for the numerical abel transform," *Rev. Sci. Instrum.* **90**, 065115 (2019).
- ⁷J. Mikosch, U. Frühling, S. Trippel, D. Schwalm, M. Weidemüller, and R. Wester, "Velocity map imaging of ion-molecule reactive scattering: The Ar⁺ + N₂ charge transfer reaction," *Phys. Chem. Chem. Phys.* **8**, 2990–2999 (2006).
- ⁸N. Kundu, V. Kumar, and D. Nandi, "Breakdown of dipole born approximation and the role of rydberg's predissociation for the electron-induced ion-pair dissociation to oxygen in the presence of background gases," *J. Chem. Phys.* **158** (2023), 10.1063/5.0141973.
- ⁹C. R. Gebhardt, T. P. Rakitzis, P. C. Samartzis, V. Ladopoulos, and T. N. Kitsopoulos, "Slice imaging: A new approach to ion imaging and velocity mapping," *Rev. Sci. Instrum.* **72**, 3848–3853 (2001).
- ¹⁰D. Townsend, M. P. Minitti, and A. G. Suits, "Direct current slice imaging," *Rev. Sci. Instrum.* **74**, 2530–2539 (2003).
- ¹¹J. J. Lin, J. Zhou, W. Shiu, and K. Liu, "Application of time-sliced ion velocity imaging to crossed molecular beam experiments," *Rev. Sci. Instrum.* **74**, 2495–2500 (2003).
- ¹²M. Wollenhaupt, M. Krug, J. Köhler, T. Bayer, C. Sarpe-Tudoran, and T. Baumert, "Three-dimensional tomographic reconstruction of ultrashort free electron wave packets," *Appl. Phys. B: Lasers Opt.* **95**, 647–651 (2009).
- ¹³C. Sparling and D. Townsend, "Tomographic reconstruction techniques optimized for velocity-map imaging applications," *J. Chem. Phys.* **157**, 114201 (2022).
- ¹⁴C. Sparling, D. Rajak, V. Blanchet, Y. Mairesse, and D. Townsend, "Fourier-hankel-abel nyquist-limited tomography: A spherical harmonic basis function approach to tomographic velocity-map image reconstruction," *Rev. Sci. Instrum.* **95** (2024), 10.1063/5.0206415.
- ¹⁵D. Strasser, X. Urbain, H. B. Pedersen, N. Altstein, O. Heber, R. Wester, K. G. Bhushan, and D. Zajfman, "An innovative approach to multiparticle three-dimensional imaging," *Rev. Sci. Instrum.* **71**, 3092–3098 (2000).
- ¹⁶A. Zhao, M. van Beuzekom, B. Bouwens, D. Byelov, I. Chakraborty, C. Cheng, E. Maddox, A. Nomerotski, P. Svihra, J. Visser, V. Vrba, and T. Weinacht, "Coincidence velocity map imaging using Tpx3Cam, a time stamping optical camera with 1.5 ns timing resolution," *Rev. Sci. Instrum.* **88**, 113104 (2017).
- ¹⁷A. T. Clark, J. P. Crooks, I. Sedgwick, R. Turchetta, J. W. L. Lee, J. J. John, E. S. Wilman, L. Hill, E. Halford, C. S. Slater, B. Winter, W. H. Yuen, S. H. Gardiner, M. L. Lipciuc, M. Brouard, A. Nomerotski, and C. Vallance, "Multimass velocity-map imaging with the pixel imaging mass spectrometry (PIImMS) sensor: an ultra-fast event-triggered camera for particle imaging," *J. Phys. Chem. A* **116**, 10897–10903 (2012).
- ¹⁸R. Wester, "Velocity map imaging of ion-molecule reactions," *Phys. Chem. Chem. Phys.* **16**, 396–405 (2014).
- ¹⁹G. Basnayake, Y. Ranathunga, S. K. Lee, and W. Li, "Three-dimensional (3D) velocity map imaging: from technique to application," *J. Phys. B: At. Mol. Opt. Phys.* **55**, 023001 (2022).
- ²⁰E. S. Goudreau, A. E. Boguslavskiy, D. J. Moffatt, V. Makhija, M. Hemsworth, R. Lausten, C. Marceau, I. Wilkinson, and A. Stolow, "Time-stretched multi-hit 3D velocity map imaging of photoelectrons," *Rev. Sci. Instrum.* **94** (2023), 10.1063/5.0149897.
- ²¹A. Vredenburg, W. G. Roeterdink, and M. H. M. Janssen, "A photoelectron-photoion coincidence imaging apparatus for femtosecond time-resolved molecular dynamics with electron time-of-flight resolution of $\sigma = 18$ ps and energy resolution $\Delta E/E = 3.5\%$," *Rev. Sci. Instrum.* **79**, 063108 (2008).
- ²²D. Rösch, R. Almeida, B. Sztáray, and D. L. Osborn, "High-resolution double velocity map imaging photoelectron photoion coincidence spectrometer for gas-phase reaction kinetics," *J. Phys. Chem. A* **126**, 1761–1774 (2022).
- ²³D. W. Chandler and P. L. Houston, "Two-dimensional imaging of state-selected photodissociation products detected by multiphoton ionization," *J. Chem. Phys.* **87**, 1445–1447 (1987).
- ²⁴W. C. Wiley and I. H. McLaren, "Time-of-flight mass spectrometer with improved resolution," *Rev. Sci. Instrum.* **26**, 1150–1157 (1955).
- ²⁵I. León, Z. Yang, and L.-S. Wang, "High resolution photoelectron imaging of Au₂⁻," *J. Chem. Phys.* **138**, 184304 (2013).
- ²⁶I. León, Z. Yang, H.-T. Liu, and L.-S. Wang, "The design and construction of a high-resolution velocity-map imaging apparatus for photoelectron spectroscopy studies of size-selected clusters," *Rev. Sci. Instrum.* **85**, 083106 (2014).
- ²⁷V. Plomp, Z. Gao, and S. Y. T. van de Meerakker, "A velocity map imaging apparatus optimised for high-resolution crossed molecular beam experiments," *Mol. Phys.* **119**, e1814437 (2021).
- ²⁸N. G. Kling, D. Paul, A. Gura, G. Laurent, S. De, H. Li, Z. Wang, B. Ahn, C. H. Kim, T. K. Kim, I. V. Litvinyuk, C. L. Cocke, I. Ben-Itzhak, D. Kim, and M. F. Kling, "Thick-lens velocity-map imaging spectrometer with high resolution for high-energy charged particles," *J. Instrum.* **9**, P05005 (2014).
- ²⁹S. Li, E. G. Champenois, R. Coffee, Z. Guo, K. Hegazy, A. Kamalov, A. Natan, J. O'Neal, T. Osipov, M. Owens, D. Ray, D. Rich, P. Walter, A. Marinelli, and J. P. Cryan, "A co-axial velocity map imaging spectrometer for electrons," *AIP Adv.* **8** (2018), 10.1063/1.5046192.
- ³⁰H. L. Offerhaus, C. Nicole, F. Lepine, C. Bordas, F. Rosca-Pruna, and M. J. J. Vrakking, "A magnifying lens for velocity map imaging of electrons and ions," *Rev. Sci. Instrum.* **72**, 3245–3248 (2001).
- ³¹A. S. Stodolna, A. Rouzée, F. Lépine, S. Cohen, F. Robicheaux, A. Gijsbertsen, J. H. Jungmann, C. Bordas, and M. J. J. Vrakking, "Hydrogen atoms under magnification: Direct observation of the nodal structure of stark states," *Phys. Rev. Lett.* **110**, 213001 (2013).
- ³²E. Wrede, S. Laubach, S. Schulenburg, A. Brown, E. R. Wouters, A. J. Orr-Ewing, and M. N. R. Ashfold, "Continuum state spectroscopy: A high resolution ion imaging study of IBr photolysis in the wavelength range 440–685 nm," *J. Chem. Phys.* **114**, 2629–2646 (2001).
- ³³G. Gitzinger, M. E. Corrales, V. Lorient, G. A. Amaral, R. de Nalda, and L. Bañares, "A femtosecond velocity map imaging study on B-band predissociation in CH₃I. I. the band origin," *J. Chem. Phys.* **132**, 234313 (2010).
- ³⁴D. Geißler, T. Rozgonyi, J. González-Vázquez, L. González, P. Marquetand, and T. C. Weinacht, "Pulse-shape-dependent strong-field ionization viewed with velocity-map imaging," *Phys. Rev. A* **84**, 053422 (2011).
- ³⁵W. G. Roeterdink and M. H. M. Janssen, "Velocity map imaging of femtosecond photodynamics in CF₃I," *Chem. Phys. Lett.* **345**, 72–80 (2001).
- ³⁶J. L. Hansen, H. Stapelfeldt, D. Dimitrovski, M. Abu-samha, C. P. J. Martiny, and L. B. Madsen, "Time-resolved photoelectron angular distributions from strong-field ionization of rotating naphthalene molecules," *Phys. Rev. Lett.* **106**, 073001 (2011).
- ³⁷S. Minemoto, H. Shimada, K. Komatsu, W. Komatsubara, T. Majima, S. Miyake, T. Mizuno, S. Owada, H. Sakai, T. Toghiani, M. Yabashi, P. Decleva, M. Stener, S. Tsuru, and A. Yagishita, "Time-resolved photoelectron angular distributions from nonadiabatically aligned CO₂ molecules with SX-FEL at SACLA," *J. Phys. Commun.* **2**, 115015 (2018).
- ³⁸C. Lux, M. Wollenhaupt, T. Bolze, Q. Liang, J. Köhler, C. Sarpe, and T. Baumert, "Circular dichroism in the photoelectron angular distributions of camphor and fenchone from multiphoton ionization with femtosecond laser pulses," *Angew. Chem. Int. Ed.* **51**, 5001–5005 (2012).
- ³⁹C. Sparling and D. Townsend, "Two decades of imaging photoelectron circular dichroism: from first principles to future perspectives," *Phys. Chem. Chem. Phys.* (2025),

- 10.1039/d4cp03770g.
- ⁴⁰Y. Liu, P. Chakraborty, S. Matsika, and T. Weinacht, "Excited state dynamics of *cis,cis*-1,3-cyclooctadiene: UV pump VUV probe time-resolved photoelectron spectroscopy," *J. Chem. Phys.* **153**, 074301 (2020).
- ⁴¹D. A. Horke, G. M. Roberts, J. Lecointre, and J. R. R. Verlet, "Velocity-map imaging at low extraction fields," *Rev. Sci. Instrum.* **83**, 063101 (2012).
- ⁴²B. Ding, W. Xu, R. Wu, Y. Feng, L. Tian, X. Li, J. Huang, Z. Liu, and X. Liu, "A composite velocity map imaging spectrometer for ions and 1 keV electrons at the shanghai soft x-ray free-electron laser," *Appl. Sci.* **11**, 10272 (2021).
- ⁴³Y. Ren, Z. Qin, H. Wang, X. Zheng, and Z. Cui, "An approach for improving signal-to-noise ratio in photoelectron velocity map imaging experiments," *J. Electron Spectrosc. Relat. Phenom.* **222**, 5–9 (2018).
- ⁴⁴R. M. Eastment and C. H. B. Mee, "Work function measurements on (100), (110) and (111) surfaces of aluminium," *J. Phys. F* **3**, 1738–1745 (1973).
- ⁴⁵F. Marlow, S. Josten, and S. Leiting, "Electronics with stainless steel: The work functions," *Journal of Applied Physics* **133** (2023), 10.1063/5.0142185.
- ⁴⁶P. A. Anderson, "The work function of copper," *Phys. Rev.* **76**, 388–390 (1949).
- ⁴⁷H. L. Skriver and N. M. Rosengaard, "Surface energy and work function of elemental metals," *Phys. Rev. B* **46** (1992).
- ⁴⁸J. W. Kim and A. Kim, "Absolute work function measurement by using photoelectron spectroscopy," *Curr. Appl. Phys.* **31**, 52–59 (2021).
- ⁴⁹R. Bai, N. L. Tolman, Z. Peng, and H. Liu, "Influence of atmospheric contaminants on the work function of graphite," *Langmuir : the ACS journal of surfaces and colloids* **39**, 12159–12165 (2023).
- ⁵⁰K. J. Rietwyk, D. A. Keller, A. Ginsburg, H.-N. Barad, M. Priel, K. Majhi, Z. Yan, S. Tirosh, A. Y. Anderson, L. Ley, and A. Zaban, "Universal work function of metal oxides exposed to air," *Adv. Mater. Interfaces* **6** (2019), 10.1002/admi.201802058.
- ⁵¹W. Li and D. Y. Li, "On the correlation between surface roughness and work function in copper," *J. Chem. Phys.* **122**, 064708 (2005).
- ⁵²N. Kotsina, M. Candelaresi, L. Saalbach, M. M. Zawadzki, S. W. Crane, C. Sparling, and D. Townsend, "Short-wavelength probes in time-resolved photoelectron spectroscopy: an extended view of the excited state dynamics in acetylacetone," *Phys. Chem. Chem. Phys.* **22**, 4647–4658 (2020).
- ⁵³K. Deilamian, J. D. Gillaspay, and D. E. Kelleher, "Stray-light suppression with high-collection efficiency in laser light-scattering experiments," *Appl. Opt.* **31**, 2820–2824 (1992).
- ⁵⁴E. H. Roberts, S. J. Cavanagh, S. T. Gibson, B. R. Lewis, C. J. Dedman, and G. J. Picker, "Achieving high signal-to-noise performance for a velocity-map imaging experiment," *J. Electron Spectrosc. Relat. Phenom.* **144-147**, 251–254 (2005).
- ⁵⁵K. Fehre, D. Trojanowskaja, J. Gatzke, M. Kunitski, F. Trinter, S. Zeller, L. P. H. Schmidt, J. Stohner, R. Berger, A. Czasch, O. Jagutzki, T. Jahnke, R. Dörner, and M. S. Schöffler, "Absolute ion detection efficiencies of microchannel plates and funnel microchannel plates for multi-coincidence detection," *Rev. Sci. Instrum.* **89**, 045112 (2018).
- ⁵⁶D. A. Dahl, "SIMION for the personal computer in reflection," *Int. J. Mass Spectrom.* **200**, 3–25 (2000).
- ⁵⁷S. L. Logunov and S. A. Kuchinsky, "Scattering losses in fused silica and caf 2 for duv applications," in *Optical Microlithography XVI*, SPIE Proceedings, edited by A. Yen (SPIE, 2003) p. 1396.
- ⁵⁸S. Choi, W. Shin, N. Kim, M. Kim, S. Lee, H. Jeon, and H. Lee, "Influence of storage conditions on the electronic structure of Au and interfacial state formation with C60," *Appl. Surf. Sci.* **684**, 161960 (2025).
- ⁵⁹S.-Y. Liu, K. Alnama, J. Matsumoto, K. Nishizawa, H. Kohguchi, Y.-P. Lee, and T. Suzuki, "He I ultraviolet photoelectron spectroscopy of benzene and pyridine in supersonic molecular beams using photoelectron imaging," *J. Phys. Chem. A* **115**, 2953–2965 (2011).
- ⁶⁰T. Suzuki, "Ultrafast internal conversion of aromatic molecules studied by photoelectron spectroscopy using sub-20 fs laser pulses," *Molecules* **19**, 2410–2433 (2014).
- ⁶¹Owen J. Clarkin, *Chemical Reaction Dynamics at the Statistical Ensemble and Molecular Frame Limits*, Ph.D. thesis, Queen's University (2012).
- ⁶²A. Scherer, O. T. Inal, and A. J. Singh, "Investigation of copper oxide coatings for solar selective applications," *Sol. Energy Mater.* **9**, 139–158 (1983).
- ⁶³Purnima Richharia, "Optical and microstructural analyses of a chemically converted textured black copper selective surface," *Sol. Energy Mater.* **20**, 199–214 (1990).